Comprehensive Modeling and Characterization of Photon Detection Efficiency and Jitter Tail in Advanced SPAD Devices

Remi Helleboid, Denis Rideau, Jeremy Grebot, Isobel Nicholson, Norbert Moussy, Olivier Saxod, Marie Basset, Antonin Zimmer, Bastien Mamdy, Dominique Golanski, et al.

Received 27 March 2022; revised 14 April 2022; accepted 14 April 2022. Date of publication 19 April 2022; date of current version 2 August 2022.
The review of this article was arranged by Editor L. Hutin.

Digital Object Identifier 10.1109/JEDS.2022.3168365

Comprehensive Modeling and Characterization of Photon Detection Efficiency and Jitter Tail in Advanced SPAD Devices

RÉMI HELLEBOID[1,2,3], DENIS RIDEAU[1], JEREMY GREBOT[1], ISOBEL NICHOLSON[4], NORBERT MOUSSY[2], OLIVIER SAXOD[2], MARIE BASSET[1], ANTONIN ZIMMER[1], BASTIEN MAMDY[1], DOMINIQUE GOLANSKI[1], MEGAN AGNEW[4], SARA PELLEGRINI[4] (Member, IEEE), MATHIEU SICRE[1], CHRISTEL BUJ[1], GUILLAUME MARCHAND[1], JÉRÔME SAINT-MARTIN[3], MARCO PALA[3] (Member, IEEE), AND PHILIPPE DOLLFUS[3] (Member, IEEE)

1 TDP-TOS, STMicroelectronics, 38926 Crolles, France
2 CEA LETI, 38054 Grenoble, France
3 Université Paris–Saclay, CNRS, Centre de Nanosciences et de Nanotechnologies, 91120 Palaiseau, France
4 IMG Division, STMicroelectronics, Edinburgh EH3 5DA, U.K.

CORRESPONDING AUTHOR: R. HELLEBOID (e-mail: remi.helleboid@st.com)

This work was supported in part by ECSEL JU through VIZTA Project (https://www.vizta-ecsel.eu/) under Grant 826600; in part by the French "Association Nationale Recherche Technologie" (ANRT); and in part by the French GeSPAD Project of the Agence Nationale de la Recherche under Grant ANR-20-CE24-0004.

ABSTRACT A new method to reliably simulate the PDE and jitter tail for realistic three-dimensional SPAD devices is presented. The simulation method is based on the use of electric field lines to mimic the carriers' trajectories, and on one-dimensional models for avalanche breakdown probability and charges transport. This approach allows treating a three-dimensional problem as several one-dimensional problems along each field line. The original approach is applied to the McIntyre model for avalanche breakdown probability to calculate PDE, but also for jitter prediction using a dedicated advection-diffusion model. The results obtained numerically are compared with an extensive series of measurements and show a good agreement on a wide variety of device designs.

INDEX TERMS Avalanche breakdown probability, breakdown voltage, jitter, photon detection efficiency (PDE), single-photon avalanche diode (SPAD), technology computer-aided design (TCAD).

I. INTRODUCTION AND DEVICE STRUCTURES

Single-photon Avalanche Diodes (SPAD) are key optoelectronic detectors for medical imaging, camera ranging, and automotive laser imaging detection and ranging (LiDAR) applications. Currently, the device leading the market of SPADs is a micrometric silicon (Si) PN junction associated with nearby CMOS electronics biasing the system above the breakdown voltage (BV) [1].

The main figure of merit for the sensor sensitivity is the photon detection efficiency (PDE), which is the probability that a photon hitting the SPAD is detected. It can be evaluated by multiplying the probability that an incoming photon hits the photosensitive area of the sensor, the fill factor (FF), by the probability that the photon is absorbed within the silicon volume of the sensor, the optical absorption (OA), and by the probability that the photogenerated electron-hole pair triggers an avalanche within the SPAD, the breakdown probability (BrP). This is summed up by the formula: $PDE = FF \cdot OA \cdot BrP$.

In this work, the optical absorption and the fill factor are kept constant, as they depend only on the optical stack and the read-out circuit. The modeling and optimization work are focused on the avalanche breakdown probability. Yet the model validation can only be made by PDE comparison which is the only figure that can be characterized.

Si-SPADs are suitable for mass production because of their low cost, their compatibility with CMOS process and their relatively good sensitivity and noise performances in the visible light spectrum [2]–[4]. Yet several applications, such as automotive LiDAR, require for the SPAD to be operated in the near infrared region (NIR) [5]. As the silicon absorption rate is rather low at high light wavelengths, it is

critical to optimize the PDE for these applications [6]–[8]. This must be done by engineering the device layout and process without compromising the timing characteristics, in particular the timing jitter.

It is therefore necessary to be able to iterate design improvements without waiting for silicon fabrication, which requires predictive modeling. A great deal of effort is ongoing in the SPAD simulation community to find accurate methodologies. The state-of-the-art in PDE and jitter prediction relies on Monte Carlo simulation which is computationally extremely expensive [9]–[12]. In this paper we introduce an alternative technique, combining the McIntyre model [13] with analytical simulation of the jitter tail [14]. Recent works explored the statistical fluctuation of the avalanche process together with a study on SPAD's time resolution [15], [16]. This is achieved by performing computations along the electric field lines, allowing for three-dimensional simulation and providing an accurate forecasting of the PDE and jitter tail for a given layout. The computational efficiency of this approach allows high resolution mapping at several temperatures and biases in a time frame compatible with industrial TCAD needs. Indeed, several months are necessary to manufacture and characterize a SPAD device. Thus, an optimization procedure based only on manufactured devices would be too slow and very expensive. Our method makes it possible to scale down the iterative optimization process down to less than a week.

This modeling strategy is validated on a variety of SPAD architectures. These architectures are engineered such that each layout creates a different electric field profile varying both laterally and vertically within the volume of the device. They were then manufactured on silicon and characterized using a methodology which prevents distortion of results from any potential crosstalk and additional parasitic effects by enabling only one SPAD pixel among the several pixels in an array composing a full sensor.

The SPAD devices used to test our modeling approach are based on a silicon n-on-p junction. These architectures consist of p-type and n-type doped regions, forming the main junction, also called avalanche region. In addition, a guard ring, which is made of peripheral annular regions of lower p-type and n-type doping is designed to prevent lateral breakdown [17], [18]. Additional high doping at the electrodes allows us to achieve low Ohmic contact resistance. At the backside, the interface with the optical stack is passivated, a high p doping layer allows us to enhance the recombination of carriers created from interface defects [8], [19]. A schematic representation of the SPAD architecture is shown in Figure 1.

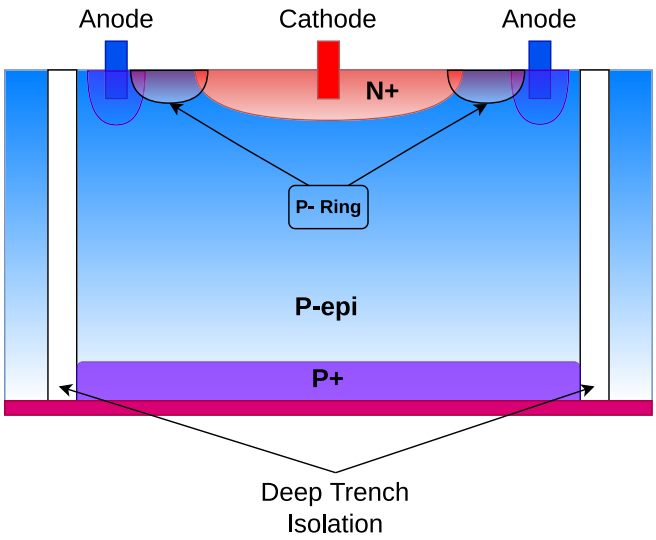

FIGURE 1. SPAD schematic architecture.

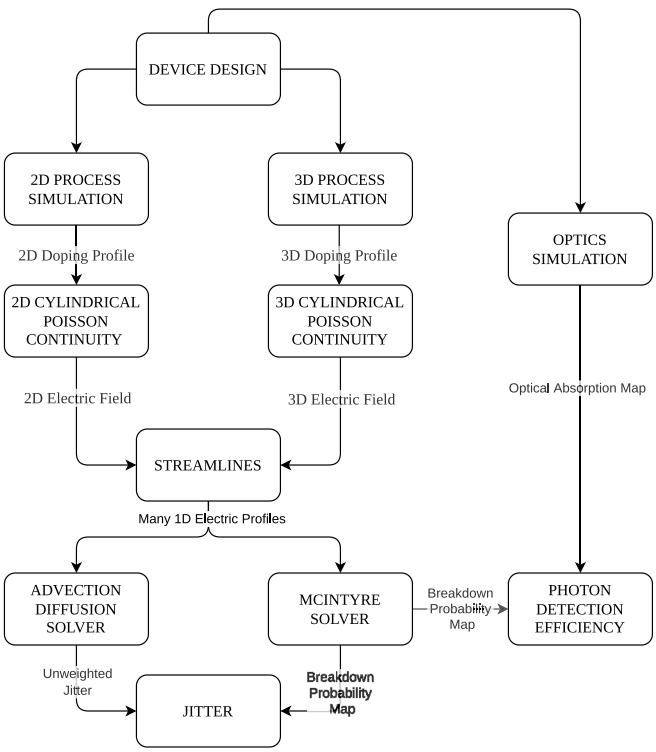

FIGURE 2. Workflow of the simulation process.

II. AVALANCHE BREAKDOWN PROBABILITY

A. PROCESS AND DEVICE TCAD SIMULATION

The structures' doping profiles were modeled with a well-calibrated process using Sentaurus Process. This is followed by electrostatic device simulation with Sentaurus Device. The 2D/3D electric field profiles are interfaced with custom solvers developed to calculate carrier trajectories, breakdown probability and jitter distribution. In parallel, optical simulation with the well-known Finite Difference Time Domain (FDTD) solver of Lumerical was performed on the architectures to obtain maps of optical absorption. The back end of the devices including the microlens and the full optical stack was kept constant for comparison purposes.

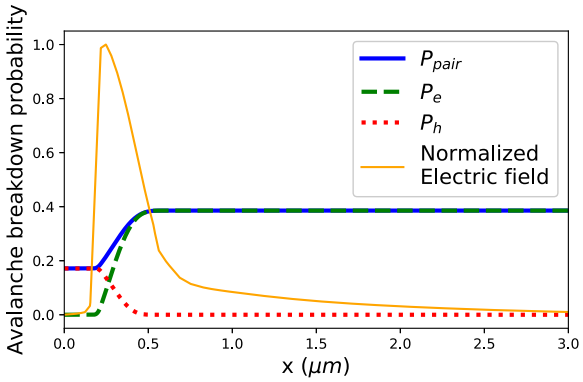

FIGURE 3. Typical solution of the McIntyre model as a function of position *x*, along the field line, for a given electric field profile.

B. BREAKDOWN PROBABILITY MODEL

The avalanche breakdown probability is computed by means of the well-known McIntyre model [20]. Let $P_e(x)$ be the probability that a photogenerated electron starting at any point x on a line within the device volume triggers an avalanche and $P_h(x)$ the same probability for a hole starting from the same initial position. Section II-D is devoted to describe the way to take a relevant line within the three-dimensional device. The system to be solved is written as follows:

$$\begin{cases} \dfrac{dP_e}{dx} = (1 - P_e)\alpha_e(P_e + P_h - P_eP_h) & (1) \\ \dfrac{dP_h}{dx} = -(1 - P_h)\alpha_h(P_e + P_h - P_eP_h) & (2) \end{cases}$$

with $0 \leq x \leq L$ where L is the total length of the carrier trajectory. α_e and α_h are the impact ionization coefficients, i.e., the number of impact ionization per unit distance, respectively for electrons and holes. Electrons are moving towards decreasing x (i.e., from right to left with respect to Figure 3), and are collected at $x = 0$, thus the probability for an electron to create an avalanche after being injected at $x = 0$ is zero. The same reasoning applies to holes at $x = L$. These considerations lead to the following boundary conditions:

$$\begin{cases} P_e(x = 0) = 0 & (3) \\ P_h(x = L) = 0 & (4) \end{cases}$$

Equations (1-2) together with boundary conditions (3-4) are forming a 1D, coupled, non-linear, boundary value problem.

Since we have to extract P_e and P_h values for numerous points, we used a custom solver, embedded in a C++ program.

C. NUMERICAL INTEGRATION WITH NEWTON'S METHOD

Our solver uses finite difference method coupled with a Newton's method to handle the non-linearity of the problem [21]. The algorithm is different from those implemented in MATLAB routine *(bvp4c)* or SciPy function *(solve_bvp)* [22], as they use a collocation method instead of a Newton scheme, but the comparison with these tools show no difference in the solution values.

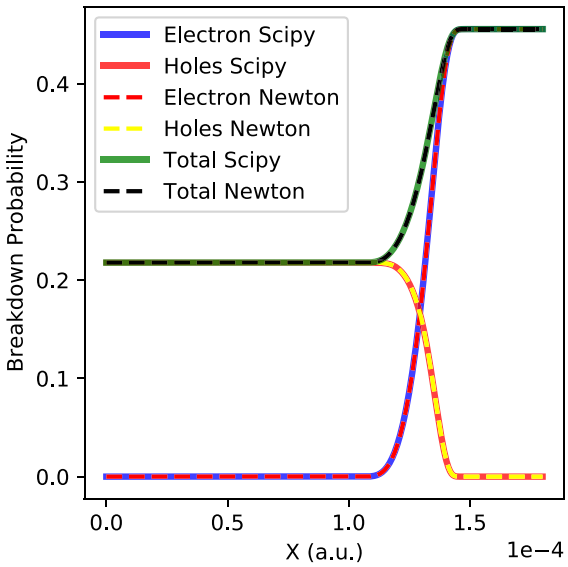

FIGURE 4. Comparison of Newton's method against the SciPy routine. Our algorithm can achieve arbitrary precision while SciPy and MATLAB routines are limited to approximately 10^{-6}. This can negatively affect breakdown voltage extraction where very small breakdown probability must be simulated accurately.

The main advantage of the Newton's method is that one can achieve arbitrary precision up to the machine precision, around 10^{-15}, with a very reasonable time consumption.

Numerical details of the solver together with a pseudocode version of the solver algorithm (Algorithm 1) are given in the Appendix. In order to check the implementation of our algorithm, we performed a comparison between the solution given by SciPy routine *solve_bvp* and our custom implementation. The comparison was made on the same electric field profile, and the results compared, see Figure 4. Furthermore, to verify the convergence of our scheme, that is, its error is decreasing when the discretization step decreases, a comparison between solutions on the same electric field profile, for different discretization steps, was done, see Figure 5.

D. APPLICATION TO THREE-DIMENSIONAL SIMULATIONS

The original McIntyre model is a purely one-dimensional model where the paths of electrons and holes are assumed to be straight lines. Often, these lines are taken from the bottom to the top of the device (see for example [23]). This work presents a method which enables the extension of the breakdown probability prediction to the entire three-dimensional or two-dimensional device simulation. For that purpose, the carrier trajectories are approximated by the field lines of the electric field. The carriers move within the device along these lines from the point of optical generation to the avalanche region. This is performed both forward (hole motion) and backward (electron motion) with respect to the electric field

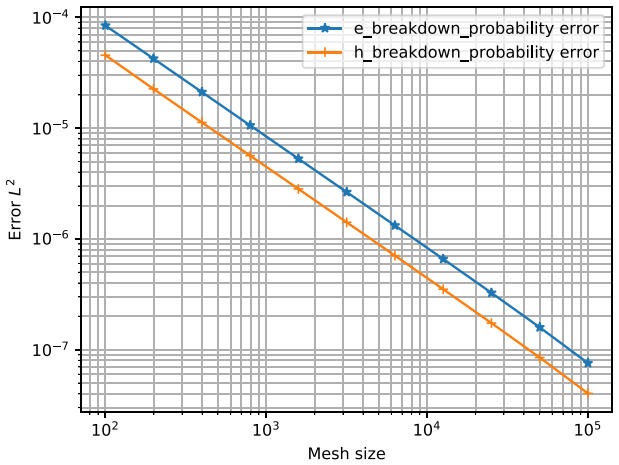

FIGURE 5. **Convergence rate of the method increasing the number of discretization points. The linear rate is consistent with the first order discretization used in the finite difference scheme.**

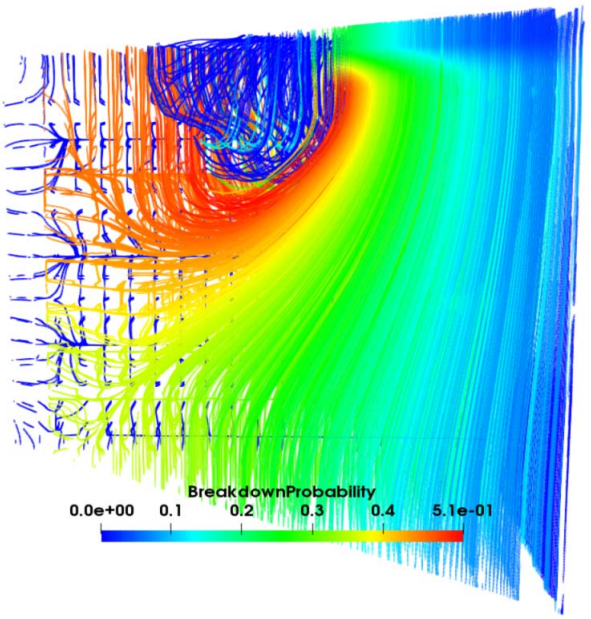

FIGURE 6. **Breakdown Probability computed over multiple field lines. These field lines are computed along the electric field and mimic the individual carriers trajectories from the departure at the point of photo-generation up to the junction. For accurate three-dimensional calculation of breakdown probability, a great number of calculations is needed (typically 500 000). For the purpose of visualization only 8000 are shown in this figure.**

vector. The electric field norm is then interpolated along the resulting field line, obtaining a detailed profile of the electric field along the carrier trajectory. A typical example of this is shown in Figure 3. The field dependent, local, impact ionization coefficients, which are the number of impact ionization events undergone by a carrier at a given electric field, are taken from the work of Van Overstraeten and De Man [24]. The need of using a non-local models for these coefficients is still under debate; some authors [23] found good agreement with experiments using local models while other authors claimed that a non-local model is needed [13]. Non-local models can be implemented consistently with our field lines methodology using an *effective* electric field model [25].

$$\frac{dP(x)}{dx} = \frac{\vec{F}_{electric}}{\|\vec{F}_{electric}\|} \tag{5}$$

Each streamline is defined by the set $\{P(x) \in \mathbb{R}^3$ for $x \in [x_min, x_final]\}$ and the Euler method then reads:

$$\frac{P(x+\delta x) - P(x)}{\delta x} = \frac{\vec{F}_{electric}(P(x))}{\|\vec{F}_{electric}(P(x))\|}$$
$$\implies P(x+\delta x) = P(x) + \delta x \frac{\vec{F}_{electric}(P(x))}{\|\vec{F}_{electric}(P(x))\|} \tag{6}$$

So, from an initial point P_0, the field lines points are iteratively constructed according to the scheme 6. The field line is then made of points, uniformly spaced by a distance δx, typically taken in a range from 1 nm to 10 nm. For an accurate three-dimensional device simulation, the calculation of about 500 000 field lines and the calculation of the associated breakdown probability are required. This can be achieved in a reasonable amount of time (20 minutes over 32 CPUs) for lines made of approximately 3000 mesh points. Figure 6 shows a subset of these lines (8000) on a clip of a SPAD device.

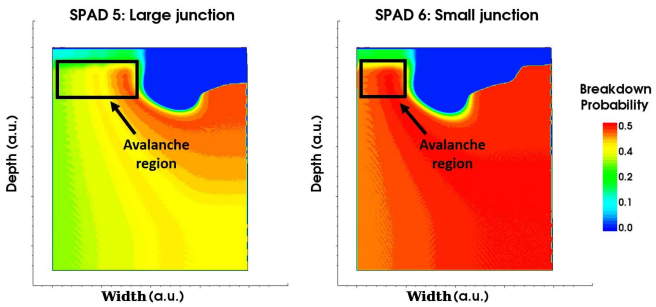

FIGURE 7. **Two-dimensional color maps of avalanche breakdown probability from two design variations with a larger and a smaller avalanche region. The value at a given point is the probability that an electron-hole pair generated at this point will eventually trigger an avalanche. Breakdown probability is shown at 4 V excess bias and 333K.**

The outcome is then gathered in maps of breakdown probability, shown in Figure 7. These maps are done by computing the breakdown probability from streamlines with starting points on a fine mesh.

The local map of avalanche breakdown probability, as shown in Figure 7, was then generated by keeping the breakdown probability value on a given set of points, well distributed over the device volume.

The breakdown probability map can be used to compute the overall PDE by coupling it with an optical absorption map. The Photon Detection Probability (PDP) is first extracted from the local breakdown probability and the local

optical absorption, by assuming:

$$PDP = \int_{V_{active}} BrP(\mathbf{r}) \cdot OA(\mathbf{r}) \mathrm{d}\mathbf{r} \tag{7}$$

where V_{active} is the photosensitive volume of the SPAD. Finally, the PDE is obtained by scaling down the PDP by the fill factor: $PDE = PDP * FF$.

This local assessment of the breakdown probability is also mandatory to simulate SPAD dark count rate from generation-recombination rates [26].

III. JITTER MODELING

The jitter in SPAD devices is related to the timing between the arrival of the photon and the detection of the avalanche signal. The jitter is usually defined as the Full-Width at Half-Maximum (FWHM) statistical distribution of time to detect avalanche breakdown, but the distribution tail is also of essential importance as it can impact the time of flight measurement accuracy. Jitter can be inferred from the avalanche build up time itself [10], but also from the carrier transit time within the device toward the junction [27]. While the build up typically occurs within a few tens of picoseconds, the carrier drift and diffusion can be longer, especially for SPADs in which a large collection region extends beyond the high field avalanche region [28].

The present work focuses on the modeling of the carrier transport part which is responsible for the tail of the jitter distribution. This means that the statistical distribution of the build-up time is not taken into account in this work. This limitation prevents us from being able to accurately predict the shape of the initial peak of the jitter histogram. Yet we are able to model the tail of the timing distribution which is due to the drift and diffusion of carriers from their photogenerated location to the average avalanche location.

A photon absorbed at a given point $\mathbf{r_0}$ leads to the creation of an electron-hole pair and for an accurate jitter calculation one needs to model the statistical distribution of time taken for the electron (respectively hole) to reach the avalanche region (represented by the position of the maximum electric field, denoted $x_{E_{max}}$). To do so, the field lines and the one dimensional advection-diffusion equation with variable velocity and diffusion are coupled. We assume that the electron will drift and diffuse along the electric field line (neglecting transverse diffusion) with starting point $\mathbf{r_0}$ in the real-space, which corresponds to the point x_0, along the field line.

Following Jacoboni and Lugli [29], in the low-to-moderate field regions, the solution of the advection-diffusion equation can be used to model the density probability $f : (x, t) \mapsto f(x, t)$ of having an electron at position x and time t when injected at $x = x_0$ at $t = 0$. The equation reads:

$$\frac{\partial f}{\partial t}(x,t) = -\frac{\partial (u \cdot f)}{\partial x}(x,t) + \frac{\partial}{\partial x}\left(D \cdot \frac{\partial f}{\partial x}\right)(x,t) \tag{8}$$

At time $t = 0$, f is a Dirac distribution function, localized at the photon absorption position. However, in order to compute a solution numerically, we start at a time $t_0 = \delta t$ where

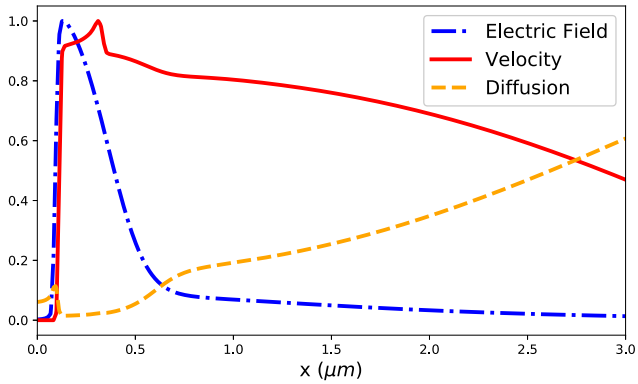

FIGURE 8. Normalized electric field, electron velocity and diffusion coefficient along a field line (see text for details).

$\delta t \approx 10^{-12}$. During δt, we can approximate $D(x) = D(x_0)$ and $u(x) = u(x_0)$, and use the analytical solution of the one dimensional advection-diffusion equation with constant velocity and diffusion coefficients:

$$f(x, t = t_0) = \frac{1}{\sqrt{4\pi D(x_0) t_0}} \exp\left(-\frac{((x - x_0) - v(x_0)t_0)^2}{4D(x_0)t_0}\right) \tag{9}$$

Additionally, we set an absorbing boundary condition at $x = x_{E_{max}}$. Indeed, we consider that the main avalanche is occurring close to the maximum of the electric field. The absorbing boundary condition reads:

$$\frac{\partial f}{\partial t}(x_{E_{max}}, t) = \frac{\partial}{\partial x}\left(D \cdot \frac{\partial f}{\partial x}\right)(x_{E_{max}}, t) \tag{10}$$

The carrier velocity is computed with a high field saturation model and the diffusion through the Einstein relation $D = \frac{\mu k_B T}{q}$. These quantities are represented in Figure 8. Let T_e be the time for the electron to reach the avalanche region. The probability that T_e is less than t is:

$$\mathbb{P}(t < T_e) = F_{T_e}(t) = 1 - \int_{x_{min}}^{x_{max}} f(x, t) dx$$

From this cumulative distribution function, the distribution function of T can be retrieved:

$$f_T(t) = \frac{dF_{T_e}(t)}{dt} \tag{11}$$

The same equation also applies to holes taking the hole velocity and diffusion. Equation 8 is solved by the mean of the finite difference method, within a modified Crank-Nicolson scheme that takes into account the variable velocity and diffusion. The Crank-Nicolson scheme results in a linear system to solve at each time iteration, a complete simulation can take up to 100 000 iterations, depending on the time step dt. The sparsity of the linear system and the possibility to perform a factorization of the system's matrix only once at the first iteration makes the computation time reasonable even for complex full three-dimensional structures. This jitter

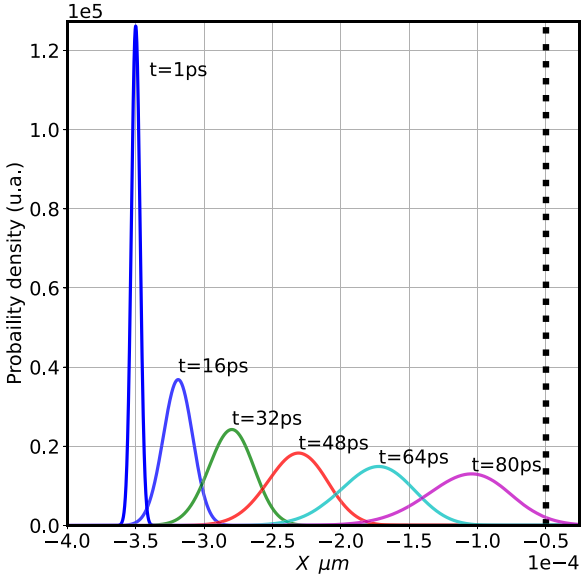

FIGURE 9. **Illustration of the Jitter modeling. The density probability function of an electron is both transported and diffused. The dashed line represents the "avalanche region".**

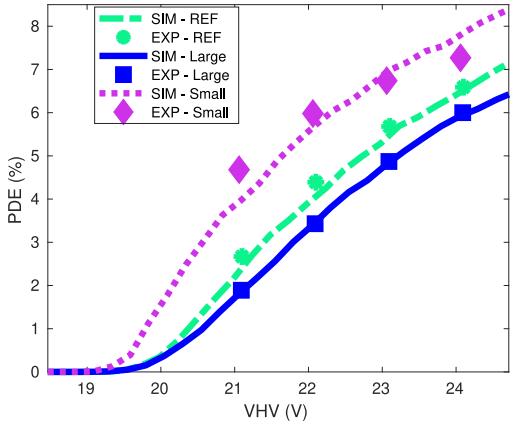

FIGURE 10. **Comparison of PDE measured and simulated on three architecture variations at 333K. The three diodes have varying sizes of junction radius, corresponding to SPADs Ref, 5 and 6 of Figures 12 and 11. The large and small architectures correspond to those shown in Figure 7.**

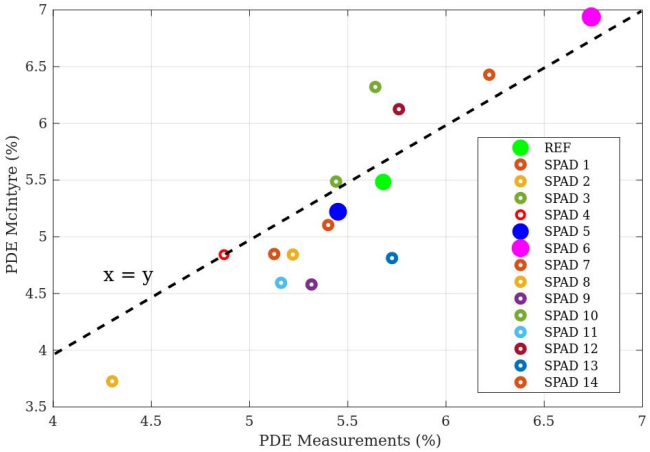

FIGURE 11. **Correlation between simulation and experiment for PDE at 4 V excess bias with a temperature of 333K for 15 diodes of varying architecture.**

calculation adds approximately 20 more minutes of computation time (using 32 CPUs) to the previously mentioned breakdown probability calculations.

IV. RESULTS AND COMPARISONS WITH EXPERIMENTS

To validate our models, the simulation results were compared with experimental measurements performed on the wide range of architecture variants described in Section I. PDE measurements are repeated on several SPADs to reduce the variability of the results and the values given are the median ones.

We first present the PDE results derived from the avalanche breakdown probability simulations described in Section II. A key visualization of the result is the breakdown probability color map, which is generated for two different architectures with different junction sizes in Figure 7.

This figure shows a higher PDE for the smaller junction area. By engineering the doping profile, it is indeed possible to focus the electric field lines in a region with a higher electric field, and thus increase the probability of triggering an avalanche [8]. This can be done for example by reducing the lateral extension of the N+ doping region (see Figure 1). To verify that this prediction is physical, the integrated PDE for a range of voltages can be extracted. The resulting curve is shown for the three architectures with junctions of various areas overlaid by the appropriate experimental results in Figure 10. The PDE values are obtained by multiplying the breakdown avalanche probability by the optical absorption. In this study, the absorption was simulated at the operational wavelength of the SPAD, 940 nm. The simulation takes into account the full optical stack and the metal reflector at the front of the device (at the contact side in Figure 1). Details of the optical simulation can be found in [30]. The outcome of the simulation is an overall of 26% of the incoming photon to be absorbed within the volume of the device, for this architecture. This value takes into account the optical fill factor of the SPAD, that is, the ratio of the sensitive area to the total SPAD area.

The comparison was extended to a large set of fifteen different architectures with electric field profiles selected for their wide range of electrostatic characteristics. As shown in Figure 11, which presents the correlation between simulation and experiment at 4V excess voltage above BV, the model was able to accurately predict a significant range of PDE correctly.

The breakdown voltage of the SPAD can also be extracted from the simulation of the breakdown probability at different applied voltage biases. We define that the device has entered the avalanche regime when an arbitrary threshold PDE of 10^{-5} is reached, the BV is then the lowest applied voltage for which the threshold is reached. The BV extraction was performed on the same fifteen diodes and the results, shown

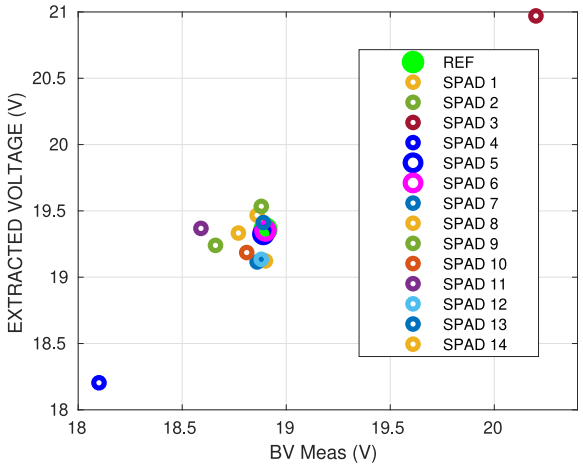

FIGURE 12. **Correlation between simulation and measurements for breakdown voltage at 333K for 15 diodes of varying architecture.**

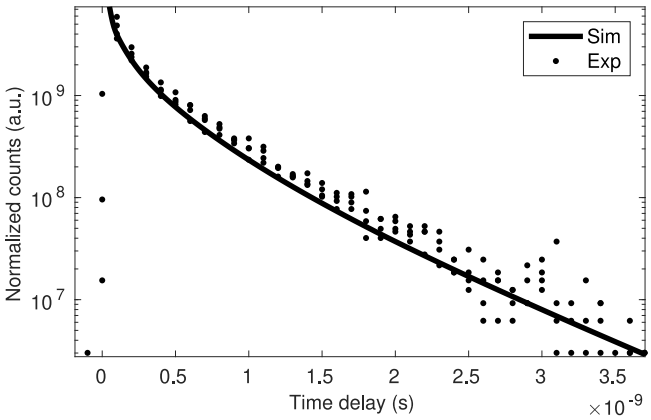

FIGURE 13. **Comparison between characterization and simulation for jitter at 4 V excess bias and 333K. To dots corresponds to the histogram of the time delays measured. For comparison purposes, both simulation and measurements data are renormalized by the total number of counts, which is the total area of the curve. The result can then also be interpreted as a probability density function.**

in Figure 12, show the resulting correlation. In particular, the extreme breakdown voltages engineered for SPADs 3 and 4 are correctly predicted by the model.

Finally, a comparison between characterization and simulation was made for the jitter model. Figure 13 shows the tail of the jitter simulated by the model described in Section III overlaid by the corresponding experimental data for a reference diode. The good correlation is a confirmation of the jitter model's validity.

The ability of both the McIntyre and jitter models over field lines in predicting PDE, BV and jitter characteristics are essential to confirm a clear understanding of the device physics. Furthermore, it allows for confidence in design optimization in an early development phase.

V. CONCLUSION

Advanced SPADs devices have highly curved electric fields, this makes conventional use of one-dimensional avalanche breakdown probability models unusable. This problem is addressed in this work by integrating the one-dimensional McIntyre model over several field lines from several photogeneration starting points within the device. This allows for the accurate prediction of the local avalanche breakdown probability, which is converted into the photon detection efficiency by coupling it with optical simulation of the device.

The same approach is applied to predict the tail of the jitter histogram. A one-dimensional drift-diffusion model is used on the field lines to simulate the drift-diffusive transport of carriers from their absorption location to the avalanche region.

Both models are tested by performing comparison with experimental results on manufactured SPADs. Simulation shows good agreement with characterization results, which indicates that the models can be used to accurately predict PDE and jitter tail with simulations.

Algorithm 1: Newton's Method Solver for BVP

input : The Boundary value Problem
input : The Mesh $\mathcal{M}$
input : An initial guess of $U_{\mathcal{M}}$
input : A maximal tolerance TOL
input : A maximal number of iterations
output: The Solution $U_{\mathcal{M}}$
output: The final residual error

RES $\leftarrow 1e6$
NbIterations $\leftarrow 0$
Initialize $w_{\mathcal{M}}$ as a vector of size 2N

while *RES* $>$ *TOL and NbIterations* $\leq$ *MaxNbIterations* **do**
  for *i=1 to 2N* **do**
    Construct S_i Construct R_i Construct $q_i = -N_{\mathcal{M}} u_i$
  Construct A Construct β
  Solve $A w_{\mathcal{M}} = \hat{\beta}$
  for *i=1 to 2N* **do**
    $u_i \leftarrow u_i + (w_{\mathcal{M}})_i$
  RES $\leftarrow ||w_{\mathcal{M}}||$ *NbIterations* $\leftarrow$ *NbIterations* $+ 1$
if *RES* $\leq$ *TOL* **then**
  // The method has converged
  return Y
else
  // The method has not converged
  return Error: No Convergence

APPENDIX

We report in this section the details of the numerical scheme for the McIntyre model for avalanche breakdown probability integration. We denote by U the solution vector to the problem 1.

A. NEWTON SCHEME

We set the following notations:

$$U(x) = \begin{pmatrix} U_1(x) \\ U_2(x) \end{pmatrix} = \begin{pmatrix} P_e(x) \\ P_h(x) \end{pmatrix}$$

$$f(U,x) = \begin{pmatrix} (1-U_1(x))\alpha_e(U_1(x)+U_2(x)-U_1(x)U_2(x)) \\ -(1-U_2(x))\alpha_h(U_1(x)+U_2(x)-U_1(x)U_2(x)) \end{pmatrix}$$

The boundary conditions are given under the following form:

$$\mathbf{g}(s_1, s_2) = \begin{pmatrix} s_1 \\ s_2 \end{pmatrix}$$

The problem (1 - 4) hence reads:

$$\begin{cases} U'(x) = f(U,x) & (12) \\ \mathbf{g}(U(0), U(w)) = 0 & (13) \end{cases}$$

where the derivative on U is the element wise derivative of the vector U, i.e., $(U'(x))_k = U_k(x)'$.

A.1. FINITE DIFFERENCES APPROXIMATION

From a given field line, i.e., a list of three-dimensional points

$$P_i = (P_x, P_y, P_z)_i,\ i \in [1, \ldots, N+1]$$

one can construct the one dimensional line given by $x_1 = 0$ and

$$x_{i+1} = x_i + \left|\left|\overrightarrow{P_{i+1} - P_i}\right|\right|,\ i \in [1, \ldots, N+1].$$

Hence, the 1-dimensional mesh $\mathcal{M}$ on which the problem is solved is:

$$\mathcal{M} : 0 = x_1 < x_2 < x_3 < \cdots < x_N < x_{N+1} = w$$

So that w is the total length of the field line. The approximated solution on the mesh $\mathcal{M}$ is $U_{\mathcal{M}} = (u_1, u_2, \ldots, u_N, u_{N+1})$, where u_i is the approximation of $U(x_i)$.

For numerical approximation, we again consider the mesh $\mathcal{M}$ and denote the vector of approximate solution values at mesh points by $U_{\mathcal{M}}$. The trapezoidal scheme of finite difference method is given by:

$$\begin{cases} \dfrac{u_{i+1}-u_i}{h_i} = \dfrac{1}{2}(f(x_{i+1}, u_{i+1}) + f(x_i, u_i)) & (14) \\ \mathbf{g}(u_1, u_{N+1}) = 0 & (15) \end{cases}$$

with $i \in [1, \ldots, N]$ in equation (14).

Thus, we obtain a system of $2(N+1)$ algebraic equations for the $2(N+1)$ unknowns $U_{\mathcal{M}}$. Unlike before, though, these equations are non-linear. The number N depends on the precision we take when we construct the streamlines. We commonly take a range from 1 nm to 10 nm for the distance between to consecutive field line points, resulting in $N \sim 5000$.

The Jacobian matrix of this system is rather sparse, which enables the use of a specialized sparse linear algebra solver [31] that accelerates the computation of the solution.

A.2. NEWTON'S METHOD

We consider a system of equations, with unknown s, written in the compact form:

$$\mathbf{F}(\mathbf{s}) = \mathbf{0}$$

We define a function $\mathbf{G}$:

$$\mathbf{G}(\mathbf{s}) = \mathbf{s} - \left[\mathbf{F}'(\mathbf{s})\right]^{-1}\mathbf{F}(\mathbf{s})$$

with $\mathbf{F}'(\mathbf{s})^{-1}$ the inverse of the Jacobian matrix of F:

$$\mathbf{F}'(\mathbf{s}) = \frac{\partial \mathbf{F}(\mathbf{s})}{\partial \mathbf{s}}$$

Then the Newton's iterative method is given by:

$$\mathbf{s}^{k+1} = \mathbf{G}(\mathbf{s}^k)$$

So, the algorithm will first solve the linear system:

$$\mathbf{F}'\left(\mathbf{s}^k\right)\boldsymbol{\xi} = -\mathbf{F}\left(\mathbf{s}^k\right) \quad (16)$$

And then:

$$\mathbf{s}^{k+1} = \mathbf{s}^k + \boldsymbol{\xi} \quad (17)$$

A.3. CONSTRUCTION OF THE LINEAR SYSTEM

Let $\mathbf{N}_{\mathcal{M}}$ be the following discrete differential operator:

$$\mathbf{N}_{\mathcal{M}} u_i = \frac{u_{i+1}-u_i}{h_i} - \frac{1}{2}(f(x_{i+1}, u_{i+1}) + f(x_i, u_i))$$

Then

$$\mathbf{F}(\mathbf{s}) = \begin{pmatrix} N_{\mathcal{M}} u_1 \\ N_{\mathcal{M}} u_2 \\ \vdots \\ N_{\mathcal{M}} u_N \\ \mathbf{g}(u_1, u_{N+1}) \end{pmatrix}$$

We set

$$\boldsymbol{\xi} = \begin{pmatrix} w_1 \\ w_2 \\ \vdots \\ w_N \\ w_{N+1} \end{pmatrix}$$

So that the Newton's method iteration becomes:

$$\frac{w_{i+1}-w_i}{h_i} - \frac{1}{2}\left[A(x_{i+1})w_{i+1} + A(x_i)w_i\right] = -\mathbf{N}_{\mathcal{M}} u_i^k$$
$$1 \le i \le N$$
$$B_a w_1 + B_b w_{N+1} = -\mathbf{g}\left(u_1^m, u_{N+1}^m\right)$$

where A is the following matrix:

$$A\left(x_j\right) \coloneqq \frac{\partial f}{\partial u}\left(x_j, u_j^k\right)$$

And with

$$B_a = \frac{\partial \mathbf{g}\left(u_1^k, u_{N+1}^k\right)}{\partial s_1}, \quad B_b = \frac{\partial \mathbf{g}\left(u_1^k, u_{N+1}^k\right)}{\partial s_2}$$

which here turns into:

$$B_a = 1, \quad B_b = 1.$$

REFERENCES

[1] E. Charbon, C. Bruschini, and M.-J. Lee, "3D-stacked CMOS SPAD image sensors: Technology and applications," in *Proc. 25th IEEE Int. Conf. Electron. Circuits Syst. (ICECS)*, Dec. 2018, pp. 1–4.

[2] F. Villa *et al.*, "CMOS spads with up to 500 μm diameter and 5% detection efficiency at 420 nm," *J. Mod. Opt.*, vol. 61, no. 2, pp. 102–115, 2014.

[3] E. A. G. Webster, J. A. Richardson, L. A. Grant, D. Renshaw, and R. K. Henderson, "A single-photon avalanche diode in 90-nm CMOS imaging technology with 4% photon detection efficiency at 690 nm," *IEEE Electron Device Lett.*, vol. 33, no. 5, pp. 694–696, May 2012.

[4] M. Sanzaro, P. Gattari, F. Villa, A. Tosi, G. Croce, and F. Zappa, "Single-photon avalanche diodes in a 0.16 μm bcd technology with sharp timing response and RED-enhanced sensitivity," *IEEE J. Sel. Topics Quant. Electron.*, vol. 24, no. 2, pp. 1–9, Mar./Apr. 2018.

[5] "ANSI Z136.1-2014—American national standard for safe use of lasers." [Online]. Available: https://webstore.ansi.org/Standards/ (Accessed: Apr. 13, 2022).

[6] F. Gramuglia *et al.*, "Engineering breakdown probability profile for PDP and DCR optimization in a SPAD fabricated in a standard 55 nm BCD process," *IEEE J. Sel. Topics Quant. Electron.*, vol. 28, no. 2, pp. 1–10, Mar./Apr. 2022.

[7] E. P. Devine *et al.*, "Optimization of CMOS image sensors with single photon-trapping hole per pixel for enhanced sensitivity in near-infrared," Oct. 2021, *arXiv:2110.00206*.

[8] E. Van Sieleghem *et al.*, "A near-infrared enhanced silicon single-photon avalanche diode with a spherically uniform electric field peak," *IEEE Electron Device Lett.*, vol. 42, no. 6, pp. 879–882, Jun. 2021.

[9] D. Dolgos, H. Meier, A. Schenk, and B. Witzigmann, "Full-band Monte Carlo simulation of high-energy carrier transport in single photon avalanche diodes: Computation of breakdown probability, time to avalanche breakdown, and jitter," *J. Appl. Phys.*, vol. 110, Oct. 2011, Art. no. 84507.

[10] A. Ingargiola, M. Assanelli, A. Gallivanoni, I. Rech, M. Ghioni, and S. Cova, "Avalanche buildup and propagation effects on photon-timing jitter in Si-SPAD with non-uniform electric field," in *Proc. SPIE*, vol. 7320, May 2009, Art. no. 73200K. [Online]. Available: https://www.spiedigitallibrary.org/conference-proceedings-of-spie/7320/1/Avalanche-buildup-and-propagation-effects-on-photon-timing-jitter-in/10.1117/12.818521.short

[11] A. Gulinatti, I. Rech, M. Assanelli, M. Ghioni, and S. D. Cova, "Design-oriented simulation of the photon detection efficiency and temporal response of single photon avalanche diodes," in *Proc. IEEE LEOS Annu. Meeting Conf.*, Belek-Antalya, Turkey, Oct. 2009, pp. 297–298.

[12] T. Cazimajou *et al.*, "Quenching statistics of silicon single photon avalanche diodes," *IEEE J. Electron Devices Soc.*, vol. 9, pp. 1098–1102, 2021.

[13] L. Pancheri, D. Stoppa, and G.-F. D. Betta, "Characterization and modeling of breakdown probability in sub-micrometer CMOS SPADs," *IEEE J. Sel. Topics Quant. Electron.*, vol. 20, no. 6, pp. 328–335, Nov./Dec. 2014.

[14] R. Helleboid *et al.*, "Comprehensive modeling and characterization of photon detection efficiency and jitter in advanced spad devices," in *Proc. IEEE 51st Eur. Solid-State Device Res. Conf. (ESSDERC)*, 2021, pp. 271–274.

[15] W. Riegler and P. Windischhofer, "Time resolution and efficiency of SPADs and SiPMs for photons and charged particles," *Nucl. Instrum. Methods Phys. Res. A Accelerators Spectrometers Detectors Assoc. Equip.*, vol. 1003, Jul. 2021, Art. no. 165265. [Online]. Available: https://www.sciencedirect.com/science/article/abs/pii/S0168900221002497?via%3Dihub

[16] P. Windischhofer and W. Riegler, "The statistics of electron-hole avalanches," *Nucl. Instrum. Methods Phys. Res. A Accelerators Spectrometers Detectors Assoc. Equip.*, vol. 1003, Jul. 2021, Art. no. 165327. [Online]. Available: https://www.sciencedirect.com/science/article/pii/S0168900221003119?via%3Dihub

[17] E. Kamrani, F. Lesage, and M. Sawan, "Premature edge breakdown prevention techniques in CMOS apd fabrication," in *Proc. 10th IEEE Int. NEWCAS Conf.*, 2012, pp. 345–348.

[18] W. Wang, Y. Zhang, and Z. Wei, "High-performance structure of guard ring in avalanche diode for single photon detection," *Int. J. Commun. Netw. Syst. Sci.*, vol. 10, no. 8, pp. 1–6, Aug. 2017.

[19] M. Gersbach *et al.*, "A low-noise single-photon detector implemented in a 130nm CMOS imaging process," *Solid-State Electron.*, vol. 53, no. 7, pp. 803–808, 2009.

[20] W. G. Oldham, R. R. Samuelson, and P. Antognetti, "Triggering phenomena in avalanche diodes," *IEEE Trans. Electron Devices*, vol. ED-19, no. 9, pp. 1056–1060, Sep. 1972.

[21] U. M. Ascher, R. M. M. Mattheij, and R. D. Russell, *Numerical Solution of Boundary Value Problems for Ordinary Differential Equations*, 1st ed. Philadelphia, PA, USA: Soc. Ind. Appl. Math., Jan. 1987, pp. 194–205.

[22] J. Kierzenka and L. F. Shampine, "A BVP solver based on residual control and the MALTAB PSE," *ACM Trans. Math. Softw.*, vol. 27, no. 3, pp. 299–316, Sep. 2001.

[23] C.-A. Hsieh, C.-M. Tsai, B.-Y. Tsui, B.-J. Hsiao, and S.-D. Lin, "Photon-detection-probability simulation method for cmos single-photon avalanche diodes," *Sensors*, vol. 20, no. 2, p. 436, Jan. 2020.

[24] R. Van Overstraeten and H. De Man, "Measurement of the ionization rates in diffused silicon $p-n$ junctions," *Solid-State Electron.*, vol. 13, no. 5, pp. 583–608, May 1970.

[25] S. L. Tan, D. S. Ong, and H. K. Yow, "Theoretical analysis of breakdown probabilities and jitter in single-photon avalanche diodes," *J. Appl. Phys.*, vol. 102, no. 4, Aug. 2007, Art. no. 044506.

[26] M. Sicre *et al.*, "Dark count rate in single-photon avalanche diodes: Characterization and modeling study," in *Proc. IEEE 47th Eur. Solid-State Circuits Conf. (ESSCIRC)*, Sep. 2021, pp. 143–146.

[27] F. Sun, Y. Xu, Z. Wu, and J. Zhang, "A simple analytic modeling method for SPAD timing jitter prediction," *IEEE J. Electron Devices Soc.*, vol. 7, pp. 261–267, 2019.

[28] N. Moussy and J.-L. Ouvrier-Buffet, "Spad photodiode," Eur. Patent EP3 151 290 A1, Apr. 2017.

[29] C. Jacoboni and P. Lugli, *The Monte Carlo Method for Semiconductor Device Simulation*. Cham, Switzerland: Springer-Verlag, 1989, pp. 72–74.

[30] B. Vianne *et al.*, "Advances in 3D CMOS image sensors optical modeling: Combining realistic morphologies with FDTD," in *Proc. IEEE Int. Conf. Simulat. Semicond. Process. Devices (SISPAD)*, Udine, Italy, Sep. 2019, pp. 1–4.

[31] G. Guennebaud *et al.* "Eigen V3." 2010. [Online]. Available: http://eigen.tuxfamily.org